Characteristics of metal–uniaxial chiral–metal plasmonic waveguide structure

M. ARIF[1], M. UMAIR[1], A. GHAFFAR[1,*], MAJEED A. S. ALKANHAL[2], Y. KHAN[2], M. U. SHAHID[3]
[1]*Department of Physics, University of Agriculture, Faisalabad, Pakistan*
[2]*Department of Electrical Engineering, King Saud University, Riyadh, Saudi Arabia*
[3]*Department of Information Engineering, Electronics and Telecommunication (DIET) "La Sapienza" University of Rome, Italy*

This paper investigates the characteristics of surface plasmon polaritons (SPPs) in a planar waveguide with a uniaxial chiral (UAC) core and metal as cladding. By applying boundary conditions at $x = \pm d$, we analytically obtain the dispersion relation. Three different cases of UAC are explored as functions of the incident wave frequency. The effects of chirality (κ) and core width (w) on the effective mode index are discussed. It is observed that the effective mode index is highly sensitive when both longitudinal and transverse components of permittivity have different signs (i.e., $\varepsilon_t > 0$, $\varepsilon_z < 0$) compared to other cases. Furthermore, core width has a strong effect on the effective mode index for the proposed waveguide depending on the longitudinal and transverse components of permittivity. Field profiles are also presented to confirm the existence of SPPs. The results of the proposed waveguide reveal that the characteristics of SPPs can be tuned by controlling longitudinal and transverse permittivity, the chirality parameter, and core width. The present work may enable the nanophotonic community to fabricate novel waveguides in the THz frequency range.

1. Introduction

Surface plasmon polaritons (SPPs) are a captivating and essential phenomenon in the realm of nanophotonics and surface science [1]. They emerge at the interface between a metal and a dielectric when incident light couples with free electrons of a metal surface, leading to the formation of collective oscillations known as plasmons [2]. SPPs possess a remarkable capability to confine and propagate electromagnetic (EM) energy in spaces that are significantly smaller than the diffraction limit of light. Traditional optics is limited by the diffraction of light, which prevents the focusing of light to subwavelength dimensions. SPPs, on the other hand, can be tightly focused, allowing for the manipulation of light at the nanoscale. This has led to the development of nanophotonic devices with unprecedented capabilities, such as super-resolution imaging, optical data storage, and nanoscale light-emitting devices [3-6]. Their unique properties find practical use in various applications, including waveguide design [7], light source development [8], near-field optics utilization, surface-enhanced Raman spectroscopy (SERS) [9-11], data storage devices [12, 13], solar cell efficiency enhancement, as well as the creation of sensitive chemical sensors and biosensors [14, 15].

Many researchers have studied the interaction of EM waves in chiral media since the beginning of the 19th century. It was then realized that linearly polarized light shows optical activity when it is transmitted through these materials [16, 17]. Chiral media possess a magneto-electric coupling that distinguishes them from ordinary materials and leads to intriguing EM field properties, such as circular dichroism and optical activity. The unique behavior of chiral media has profound implications in various scientific and technological domains, contributing to the development of microwave devices such as waveguides, microwave absorbers [18], focusing/cloaking polarized antennas, and linear and circular polarization transformers [19, 20]. Unlike anisotropic media, where the constitutive parameters are represented by tensors to account for their directional dependence, isotropic chiral media do not require tensors. Instead, the constitutive parameters can be described using scalar quantities, such as circular birefringence and circular dichroism [21, 22]. The fabrication of uniaxial chiral (UAC) media involves doping parallel miniature wire spirals into a host dielectric material. The spirals must be aligned in a specific direction, and the wavelength of the SPP waves should be substantially shorter than the pitch of the wire spirals. This technique enables the creation of materials with unique optical properties, opening new avenues for advanced photonic applications. The material parameter dyadics, which are unique to anisotropic media, are the main topic of this work. The material is chiral, but the chirality only manifests along a specific axis (the z-axis in this case). Additionally, the permittivity and permeability for the z-axis differ from those of the isotropic transverse plane. These UAC media have a wide range of applications, including the microwave regime, reciprocal phase shifters, optical activity, polarization transformation, non-reflective shields and antennas, radar-absorbing layers, and circular birefringence and dichroism [23-25].

The presence of plasma-like free electrons in metals leads to a negative dielectric constant below the plasma frequency. This unique behavior of metals has significant consequences for their electrical and optical properties. Resonant coupling of the incident EM field with oscillating charges at the surface of a metal can lead to the generation of SPPs. These SPPs are formed at the interface between the metal and an adjacent dielectric material. Gold is assumed as the supporting metal in both cladding and substrate i.e. in region 1 and region 3. Here, we choose UAC as the dielectric material in region 2. Over the years, extensive research has been done on UAC slabs. For example, reflection and transmission characteristics and propagation through UAC have been studied [26]. In this paper, we investigate the characteristics of SPPs in a metal–UAC–metal waveguide, which has not yet been presented.

2. Mathematical formulation

Fig. 1 shows an illustration of the proposed model of the metal–UAC–metal waveguide. The core of the waveguide is UAC material having width w = 2d, and the cladding of the waveguide is metal. An EM wave propagates along the z-axis and attenuates along the x-axis as a function of time. Here, time dependence $e^{i\omega t}$ is implicit, with angular frequency ω. To study the SPPs in the metal–UAC–metal waveguide, we start with the constitutive relation of UAC [27].

$$\boldsymbol{D} = [\varepsilon_t \bar{\bar{I}}_t + \varepsilon_z \hat{e}_z \hat{e}_z] . \mathbf{E} - i\,\kappa\,\sqrt{\mu_0 \varepsilon_0}\,\hat{e}_z \hat{e}_z . \mathbf{H}$$
$$\boldsymbol{B} = [\mu_t \bar{\bar{I}}_t + \mu_z \hat{e}_z \hat{e}_z] . \mathbf{H} - i\,\kappa\,\sqrt{\mu_0 \varepsilon_0}\,\hat{e}_z \hat{e}_z . \mathbf{E} \tag{1}$$

The constitutive relation described in Equation (1) is defined as $\bar{\bar{I}}_t = \hat{e}_x \hat{e}_x + \hat{e}_z \hat{e}_z$. This is a dyadic vector, and κ is the chirality parameter responsible for EM coupling and chirality in the media. The permeability and permittivity of free space are denoted by μ_0 and ε_0. The transverse and longitudinal components of the permittivity and permeability of the medium are ε_t, μ_t and ε_z, μ_z, respectively. The mutually perpendicular unit vectors in the Cartesian coordinate system are $\hat{e}_x, \hat{e}_y,$ and $\hat{e}_z$.
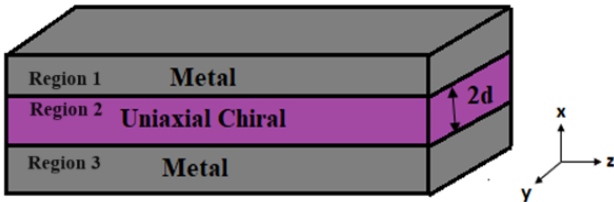

Fig. 1. Schematic illustration of metal–UAC–metal waveguide (color online)

The wave equation for the EM wave propagating along the z-axis is in region 2 given as [28]

$$\frac{\partial^2 E_z}{\partial x^2} + (p_{1,2}^2 - \beta^2)\,E_z = 0. \tag{2}$$

The solution for the above wave equation is

$$E_z = E_{z+} + E_{z-}$$

$$E_z = (A_1\,e^{q_1 x} + A_2\,e^{-q_1 x} + B_1 e^{q_2 x} + B_2\,e^{-q_2 x})\,e^{-j\beta z} \tag{3}$$

$$H_z = [\frac{i\,\alpha_1}{\eta_t}(A_1\,e^{q_1 x} + A_2\,e^{-q_1 x}) +$$
$$\frac{i\,\alpha_2}{\eta_t}(B_1 e^{q_2 x} + B_2\,e^{-q_2 x})]\,e^{-j\beta z}. \tag{4}$$

Here, $A_1, A_2, B_1,$ and B_2 are amplitudes of fields and can be found by applying boundary conditions. The EM field excited in the UAC material propagates with two different wave vectors, and the Eigen values are defined as

$$p_1^2 = \frac{\lambda^2}{2}\left[\frac{\mu_z}{\mu_t} + \frac{\varepsilon_z}{\varepsilon_t} + \sqrt{\left(\frac{\mu_z}{\mu_t} - \frac{\varepsilon_z}{\varepsilon_t}\right)^2 + \frac{4\kappa^2 \mu_z \varepsilon_z}{\mu_t \varepsilon_t}}\right] \tag{5}$$

$$p_2^2 = \frac{\lambda^2}{2}\left[\frac{\mu_z}{\mu_t} + \frac{\varepsilon_z}{\varepsilon_t} - \sqrt{\left(\frac{\mu_z}{\mu_t} - \frac{\varepsilon_z}{\varepsilon_t}\right)^2 + \frac{4\kappa^2 \mu_z \varepsilon_z}{\mu_t \varepsilon_t}}\right] \tag{6}$$

where the terms used above are defined as

$$\lambda = \sqrt{\beta^2 - \omega^2 \mu_t \varepsilon_t} \tag{7}$$

α_1 and α_2 used in equation (4) are defined below

$$\alpha_1 = \left(\frac{p_1^2}{\lambda^2} - \frac{\varepsilon_z}{\varepsilon_t}\right)\frac{\sqrt{\mu_t \varepsilon_t}}{\kappa\,\sqrt{\mu_z \varepsilon_z}} \tag{8}$$

$$\alpha_2 = \left(\frac{p_2^2}{\lambda^2} - \frac{\varepsilon_z}{\varepsilon_t}\right)\frac{\sqrt{\mu_t \varepsilon_t}}{\kappa\,\sqrt{\mu_z \varepsilon_z}} \tag{9}$$

The relation between attenuation constant q_1 and q_2 of UAC and propagation constant β is described as

$$q_1 = \sqrt{\beta^2 - p_1^2} \tag{10}$$

$$q_2 = \sqrt{\beta^2 - p_2^2} \tag{11}$$

where k_t and η_t used in equation (14) are defined as

$$k_t = \omega\sqrt{\varepsilon_t\,\mu_0} \tag{12}$$

$$\eta_t = \sqrt{\varepsilon_t/\mu_t}. \tag{13}$$

The remaining transverse electric and magnetic field components of UAC can be derived from the relation [29]

$$E_t = \left(-\frac{i\beta}{p_1^2}\nabla_t - \frac{k_t \alpha_1}{p_1^2}\,\hat{e}_z \times \nabla_t\right)E_{z+} +$$
$$\left(-\frac{i\beta}{p_2^2}\nabla_t - \frac{k_t \alpha_2}{p_2^2}\,\hat{e}_z \times \nabla_t\right)E_{z-}. \tag{14}$$

The field equations for the cladding (i.e. region 1) are described as [28]

$$E_{y1} = A_5\,e^{-\gamma_1 x}\,e^{-j\beta z} \tag{15}$$

$$H_{y1} = A_6 \, e^{-\gamma_1 x} \, e^{-j\beta z} \qquad (16)$$

$$E_{z1} = -\frac{i\gamma_1}{\omega\,\varepsilon_1} A_6 \, e^{-\gamma_1 x} \, e^{-j\beta z} \qquad (17)$$

$$H_{z1} = \frac{i\gamma_1}{\omega\,\mu_0} A_5 \, e^{-\gamma_1 x} \, e^{-j\beta z} \qquad (18)$$

Moreover, field equations for the substrate (i.e. region 3) are given as

$$E_{y3} = A_7 \, e^{\gamma_2 x} \, e^{-j\beta z} \qquad (19)$$

$$H_{y3} = A_8 \, e^{\gamma_2 x} \, e^{-j\beta z} \qquad (20)$$

$$E_{z3} = \frac{i\gamma_2}{\omega\,\varepsilon_2} A_8 \, e^{\gamma_2 x} \, e^{-j\beta z} \qquad (21)$$

$$H_{z3} = -\frac{i\gamma_2}{\omega\,\mu_0} A_7 \, e^{\gamma_2 x} \, e^{-j\beta z} \qquad (22)$$

The attenuation constant of metal (gold) is given as

$$\gamma_1 = \gamma_2 = \sqrt{\beta^2 - \omega^2 \mu_0 \, \varepsilon_m}. \qquad (23)$$

In Equation (23), ε_m is the permittivity of metal. At both metal UAC interfaces (i.e., $x = \pm d$), the following boundary conditions are applied

$$\hat{e}_x \times (E_1 - E_2) = 0 \qquad (24)$$

$$\hat{e}_x \times (H_1 - H_2) = 0. \qquad (25)$$

By applying equations (24) and (25), we obtain the dispersion relation in the form of an 8-by-8 determinant.

$$\begin{vmatrix} M11 & M12 & M13 & M14 & M15 & M16 & M17 & M18 \\ M21 & M22 & M23 & M24 & M25 & M26 & M27 & M28 \\ M31 & M32 & M33 & M34 & M35 & M36 & M37 & M38 \\ M41 & M42 & M43 & M44 & M45 & M46 & M47 & M48 \\ M51 & M52 & M53 & M54 & M55 & M56 & M57 & M58 \\ M61 & M62 & M63 & M64 & M65 & M66 & M67 & M68 \\ M71 & M72 & M73 & M74 & M75 & M76 & M77 & M78 \\ M81 & M82 & M83 & M84 & M85 & M86 & M87 & M88 \end{vmatrix} = 0$$

The above dispersion relation is defined as

$M11 = -e^{-q_1 d}$, $M12 = -e^{q_1 d}$, $M13 = -e^{-q_2 d}$,
$M14 = -e^{q_2 d}$, $M15 = e^{-\gamma_1 d}$, $M16 = 0$, $M17 = 0$,
$M18 = 0$, $M21 = -\dfrac{k_t \alpha_1 e^{-q_1 d}}{q_1}$,
$M22 = \dfrac{k_t \alpha_1 e^{q_1 d}}{q_1}$, $M23 = -\dfrac{k_t \alpha_2 e^{-q_2 d}}{q_2}$, $M24 = \dfrac{k_t \alpha_2 e^{q_2 d}}{q_2}$,
$M25 = 0$, $M26 = -\dfrac{i\mu_0 \omega e^{-\gamma_1 d}}{\gamma_1}$, $M27 = 0$, $M28 = 0$,
$M31 = -\dfrac{i\alpha_1 e^{-q_1 d}}{\eta_t}$, $M32 = -\dfrac{i\alpha_1 e^{q_1 d}}{\eta_t}$, $M33 = -\dfrac{i\alpha_2 e^{-q_2 d}}{\eta_t}$, $M34 = -\dfrac{i\alpha_2 e^{q_2 d}}{\eta_t}$, $M35 = 0$, $M36 = e^{-\gamma_1 d}$, $M37 = 0$, $M38 = 0$, $M41 = -\dfrac{ik_t \alpha_1^2 e^{-q_1 d}}{q_1 \eta_t}$,
$M42 = \dfrac{ik_t \alpha_1^2 e^{q_1 d}}{q_1 \eta_t}$, $M43 = -\dfrac{ik_t \alpha_2^2 e^{-q_2 d}}{q_2 \eta_t}$, $M44 = \dfrac{ik_t \alpha_2^2 e^{q_2 d}}{q_2 \eta_t}$, $M45 = -\dfrac{i\varepsilon_0 \omega e^{-\gamma_1 d}}{\gamma_1}$, $M46 = 0$, $M47 = 0$,
$M48 = 0$, $M51 = e^{q_1 d}$, $M52 = e^{-q_1 d}$, $M53 = e^{q_2 d}$,

$M54 = e^{-q_2 d}$, $M55 = 0$, $M56 = 0$, $M57 = -e^{-\gamma_2 d}$,
$M58 = 0$, $M61 = \dfrac{k_t \alpha_1 e^{q_1 d}}{q_1}$,
$M62 = -\dfrac{k_t \alpha_1 e^{-q_1 d}}{q_1}$, $M63 = \dfrac{k_t \alpha_2 e^{q_2 d}}{q_2}$, $M64 = -\dfrac{k_t \alpha_2 e^{-q_2 d}}{q_2}$, $M65 = 0$, $M66 = 0$, $M67 = 0$, $M68 = \dfrac{i\mu_0 \omega e^{-\gamma_2 d}}{\gamma_2}$, $M71 = \dfrac{i\alpha_1 e^{q_1 d}}{\eta_t}$, $M72 = -\dfrac{i\alpha_1 e^{-q_1 d}}{\eta_t}$,
$M73 = \dfrac{i\alpha_2 e^{q_2 d}}{\eta_t}$, $M74 = -\dfrac{i\alpha_2 e^{-q_2 d}}{\eta_t}$, $M75 = 0$,
$M76 = 0$, $M77 = 0$, $M78 = -e^{-\gamma_2 d}$, $M81 = -\dfrac{ik_t \alpha_1^2 e^{q_1 d}}{q_1 \eta_t}$, $M82 = \dfrac{ik_t \alpha_1^2 e^{-q_1 d}}{q_1 \eta_t}$, $M83 = -\dfrac{ik_t \alpha_2^2 e^{q_2 d}}{q_2 \eta_t}$,
$M84 = \dfrac{ik_t \alpha_2^2 e^{-q_2 d}}{q_2 \eta_t}$, $M85 = 0$, $M86 = 0$, $M87 = \dfrac{i\varepsilon_0 \omega e^{-\gamma_2 d}}{\gamma_2}$ and $M88 = 0$.

3. Results and discussion

This section theoretically investigates the characteristics of the SPPs in the metal–UAC–metal waveguide with the help of the above-calculated dispersion relation. SPPs propagates at both interfaces of waveguide. Mathematical derivation of both interfaces is included in dispersion relation. The effects of the chirality parameter (κ) and core width (w) on the effective mode index are discussed. Effective mode index is calculated by dividing real part of propagation constant (β) by wave number in vacuum (k_0)

Mathematically $N_{eff} = Re(\frac{\beta}{k_0})$.

Numerical results for different cases of UAC—Case I $\varepsilon_t > 0, \varepsilon_z > 0$, Case II $\varepsilon_t > 0, \varepsilon_z < 0$, and Case III $\varepsilon_t < 0, \varepsilon_z < 0$—are presented. We assume the following in our calculation: $\mu_z = \mu_t = \mu_0 = 4\,\pi \times 10^{-7}\, H/m$.

Case I: $\varepsilon_t > 0, \varepsilon_z > 0$

In this case, the effective mode index is calculated by taking $\varepsilon_z = 2.5\varepsilon_0$ and $\varepsilon_t = 3.5\varepsilon_0$. The effects of the chirality parameter (κ) and core width (w) on the effective mode index are shown in Figs. 2a and 2b, respectively. The frequency band extends from 30 to 50 THz. Fig. 2a depicts the effect of the chirality parameter (κ) on the effective mode index as a function of the incident wave frequency. The black, red, and blue lines indicate $\kappa = 0.10\ \Omega^{-1}$, $\kappa = 0.30\ \Omega^{-1}$, and $\kappa = 0.50\ \Omega^{-1}$, respectively. The figure clearly shows that the effective mode index has an inverse relationship with the chirality parameter (κ). It can be observed that as the chirality increases, the effective mode index starts decreasing and the dispersion curves are shifted toward the high-frequency region for the proposed waveguide structure. Fig. 2(b) depicts the impact of core width (w) on the effective mode index. Core width (w) varies from 150 nm to 250 nm. The figure reveals that the effective mode index has a direct relationship with core width (w) (i.e., it increases as core width (w) increases and vice versa). An increase in a waveguide's

core width (w) causes the mode field distribution to expand, which increases the effective mode index. It is possible to comprehend this by visualizing the waveguide as a confined structure that guides the EM wave along the optical axis. The effective mode index has an impact on the mode propagation properties, such as modal confinement and mode dispersion. By finely tuning the core width (w) of the waveguide, the effective mode index and behavior of the waveguide can be manipulated as needed. Moreover, it is observed that the cutoff frequency decreases as core width (w) increases. This trend indicates that increasing core width (w) reduces the operating frequency range.

index in the THz frequency band. The dispersion curves suggest that the effective mode index increases with the chirality parameter. It is also observed that the dispersion curves at chirality parameter $\kappa = 0.10 \; \Omega^{-1}$ and $\kappa = 0.30 \; \Omega^{-1}$ are closer together, whereas those at chirality parameter $\kappa = 0.30 \; \Omega^{-1}$ and $\kappa = 0.50 \; \Omega^{-1}$ are farther apart, which means that a large value of chirality has a high impact on the effective mode index. Fig. 3(b) presents the effect of core width (w) on the effective mode index. The dispersion curves in the figure suggest that the black line, which represents the core width (w) 150 nm, has a larger effective mode index than the red and blue lines, which represent the 200 nm and 250 nm core widths (w), respectively. In this graph, the blue and red lines are closer together than the black and blue lines, which means that the change in the effective mode index is more obvious at a small core width (w) than a large core width. It is of particular interest to note that the dispersion curves start shifting toward the low-frequency region for larger values of core width.
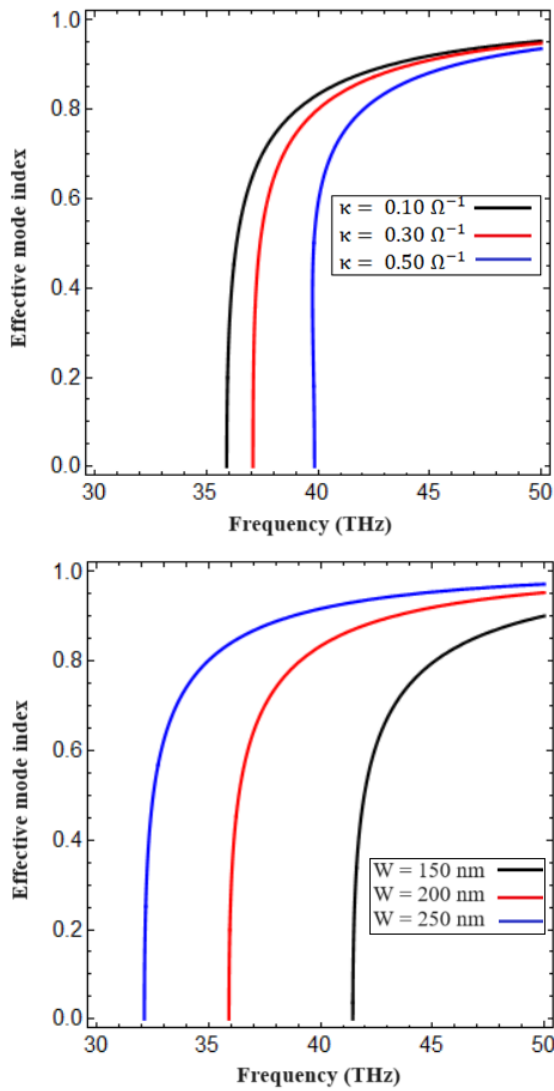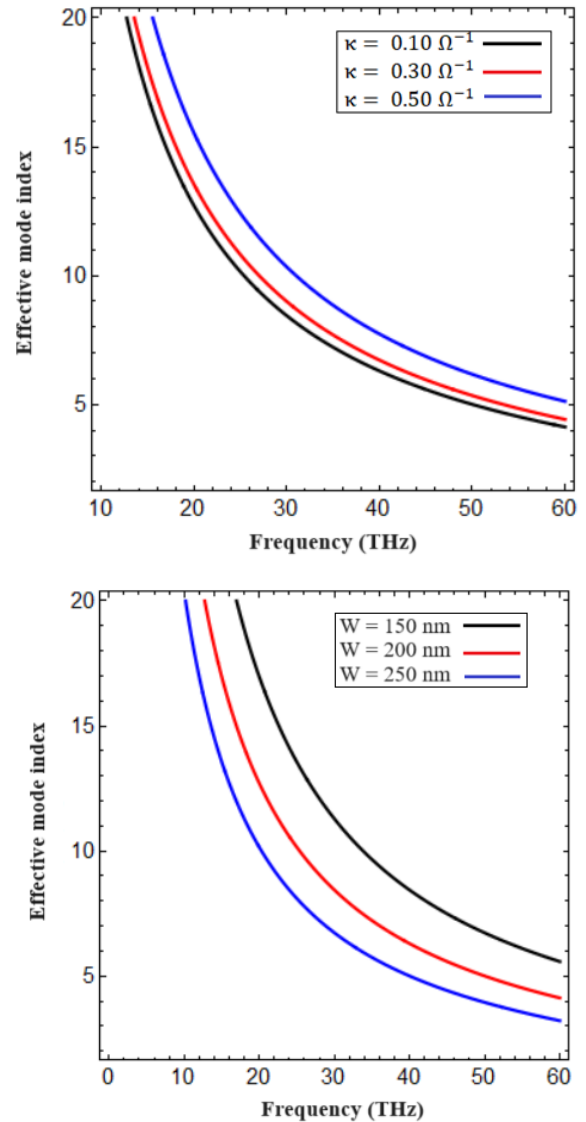

Fig. 2. Variation of effective mode index at $\varepsilon_z = 2.5\varepsilon_0$ and $\varepsilon_t = 3.5\varepsilon_0$ (a) chirality parameter (b) core width (w) (color online)

Case II: $\varepsilon_t > 0, \varepsilon_z < 0$

For this case, we take $\varepsilon_t = 1.1\varepsilon_0$ and $\varepsilon_z = -3.5\varepsilon_0$ for the metal–UAC–metal waveguide structure. Fig. 3(a) depicts the effect of chirality parameters $\kappa = 0.10 \; \Omega^{-1}$, $\kappa = 0.30 \; \Omega^{-1}$, and $\kappa = 0.50 \; \Omega^{-1}$ on the effective mode

Fig. 3. Variation of effective mode index at $\varepsilon_t = 1.1\varepsilon_0$ and $\varepsilon_z = -3.5\varepsilon_0$ (a) chirality parameter (b) core width (w) (color online)

Case III: $\varepsilon_t < 0$, $\varepsilon_z < 0$

In this case, the effective mode index is calculated by taking $\varepsilon_z = -1.5\varepsilon_0$ and $\varepsilon_t = -3\varepsilon_0$. In Fig. 4(a), chirality parameters $\kappa = 0.10\ \Omega^{-1}$, $\kappa = 0.30\ \Omega^{-1}$, and $\kappa = 0.50\ \Omega^{-1}$ are represented by black, red, and blue lines, respectively. Obviously, increasing the value of chirality parameter κ decreases the effective mode index. Moreover, the dispersion curve gaps in the graph suggest that higher values of chirality have more impact than smaller values. It is important to note that the cutoff frequency increases with the chirality. Fig. 4(b) depicts the effect of core width (w) (150 nm, 200 nm, and 250 nm) on the effective mode index. In this case, the effective mode index increases with the core width (w), whereas the cutoff frequency decreases. The cutoff frequencies are 42 THz, 48 THz, and 57 THz for core widths (w) 150 nm, 200 nm, and 250 nm, respectively. Hence, the cutoff frequency for a small core width (w) is high, which means a small core width (w) can support a higher frequency band than a large core width (w), which has a low cutoff frequency.
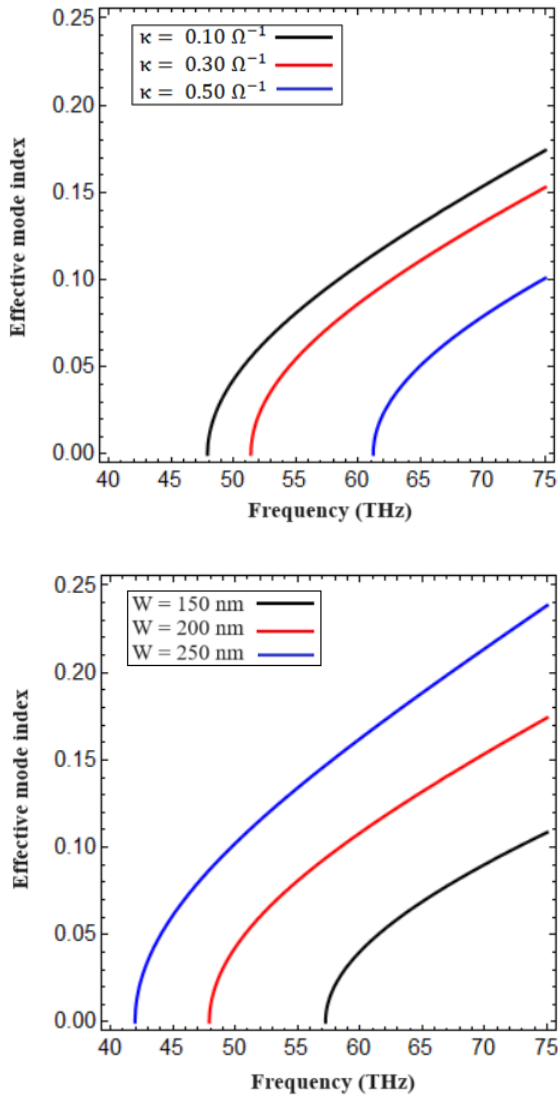
We examined the normalized field distribution of SPPs in UAC to verify the physical existence of SPPs at the interface of the proposed waveguide structure. Figs. 5a and 5b present the normalized field distribution of electric field components $|E_y|$ and $|E_z|$, while Figs. 6a and 6b illustrate the normalized field distribution of magnetic field components $|H_y|$ and $|H_z|$. Figs. 5 and 6 clearly show that the fields exponentially decay while propagating; hence, this behavior confirms the presence of SPPs in the UAC medium.
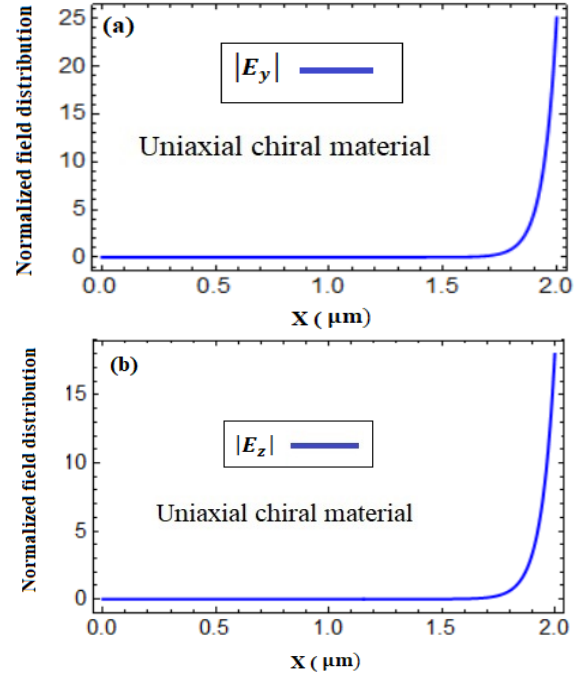

Fig. 5. Normalized field distribution of UAC material (a) (E_y) component (b) (E_Z) component (color online)
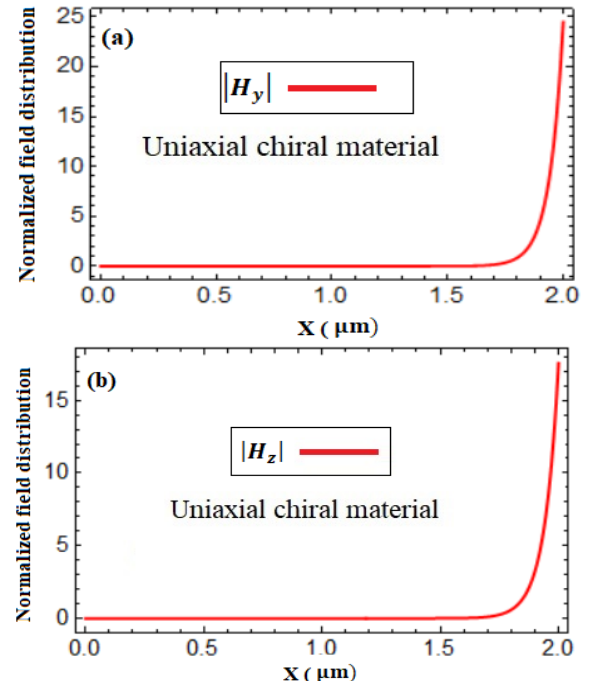

Fig. 4. Variation of effective mode index at $\varepsilon_z = -1.5\varepsilon_0$ and $\varepsilon_t = -3\varepsilon_0$ (a) chirality parameter (b) core width (color online)

Fig. 6. Normalized field distribution of UAC material (a) (H_y) component (b) (H_Z) component (color online)

4. Conclusion

The effect of the chirality parameter (κ) and core width (w) on the effective mode index for three different cases was investigated for a metal–UAC–metal waveguide structure. In the first case, both the longitudinal and transverse components of permittivity were considered as $\varepsilon_t > 0, \varepsilon_z > 0$, and it was found that the effective mode index decreased as the chirality of the material increased, whereas it increased with core width (w). In the second case, the longitudinal component of permittivity was negative and the transverse component was positive ($\varepsilon_t > 0, \varepsilon_z < 0$), and the effective mode index increased with the chirality and decreased as the core width increased. For the third case, both the longitudinal and transverse components of permittivity were taken as negative ($\varepsilon_t < 0, \varepsilon_z < 0$), and the effective mode index decreased with chirality but increased with core width (w). It is noteworthy that the effective mode index had a smaller magnitude in the first and third cases than the second case, which suggests that the effective mode index is more sensitive when permittivity components have opposite signs. Moreover, the field profile of UAC was presented to confirm the existence of SPPs. The present work may enable the plasmonics and nanophotonic community to fabricate novel waveguides in the THz frequency range.

Disclosures

The authors have no conflicts of interest to declare.

Data availability

Data underlying the results presented in this paper are not publicly available at this time but may be obtained from the authors upon reasonable request.

References

[1] J. Pitarke, V. Silkin, E. Chulkov, P. Echenique, Rep. Prog. Phys. **70**(1), 1 (2006).
[2] S. A. Maier, Plasmonics: fundamentals and applications, Springer, 2007.
[3] J. Polo, T. Mackay, A. Lakhtakia, Electromagnetic surface waves: a modern perspective, Elsevier, Newnes, 2013.
[4] B. A. Rahman, F. A. Fernandez, J. B. Davies, Proc. IEEE **79**(10), 1442 (1991).
[5] J. Sambles, G. Bradbery, F. Yang, Contem. Phys. **32**(3), 173 (1991).
[6] K. Nerkararyan, T. Abrahamyan, E. Janunts, R. Khachatryan, S. Harutyunyan, Phys. Lett. A **350**(1-2), 147 (2006).
[7] Z. Li, L. Liu, H. Sun, Y. Sun, C. Gu, X. Chen, Y. Liu, Y. Luo, Phys. Rev. Appl. **7**(4), 044028 (2017).
[8] X. Luo, L. Yan, IEEE Photonics J. **4**(2), 590 (2012).
[9] W. Lin, X. Xu, J. Quan, M. Sun, Appl. Spectrosc. Rev. **53**(10), 771 (2018).
[10] Y. Huang, Y. Fang, Z. Zhang, L. Zhu, M. Sun, Light: Sci. Appl. **3**(8), e199 (2014).
[11] J. Zhang, L. Zhang, W. Xu, J. Phys. D: Appl. Phys. **45**(11), 113001 (2012).
[12] M. L. Brongersma, P. G. Kik, Surface plasmon nanophotonics, Springer, 2007.
[13] Y. Wang, H. Liu, S. Wang, M. Cai, L. Ma, Crystals **9**(7), 354 (2019).
[14] A. Abbas, M. J. Linman, Q. Cheng, Sens. Actuators B: Chem. **156**(1), 169 (2011).
[15] A. Abbas, M. J. Linman, Q. Cheng, Biosens. Bioelectron. **26**(5), 1815 (2011).
[16] H. Cory, I. Rosenhouse, J. Mod. Opt. **38**(7), 1229 (1991).
[17] V. Fisanov, Opt. Spectrosc. **90**, 396 (2001).
[18] S. Jorwal, A. Dubey, R. Gupta, S. Agarwal, Sens. Actuators A: Phys. **354**, 114283 (2023).
[19] X. Mu, L. Hu, Y. Cheng, Y. Fang, M. Sun, Nanoscale **13**(2), 581 (2021).
[20] P. Alitalo, S. Tretyakov, Matr. Today **12**(3), 22 (2009).
[21] D. Cheng, Microw. Opt. Technol. Lett. **13**(6), 358 (1996).
[22] D. Cheng, Y. Antar, Prog. Electromagn. Res. **20**, 301 (1998).
[23] I. V. Lindell, A. H. Sihvola, IEEE Trans. Antennas Propag. **43**(12), 1397 (1995).
[24] J.-F. Dong, X.-Y. Luo, J. Li, Optoelectron. Lett. **9**(2), 148 (2013).
[25] F. Mariotte, S. A. Tretyakov, B. Sauviac, IEEE Antennas Propag. Mag. **38**(2), 22 (1996).
[26] D. Zarifi, M. Soleimani, A. Abdolali, Iran. J. Electr. Electron. Eng. **10**(4), 250 (2014).
[27] Q. Cheng, T. J. Cui, Phys. Rev. B **73**(11), 113104 (2006).
[28] M. Yaqoob, A. Ghaffar, M. Alkanhal, S. U. Rehman, F. Razzaz, Sci. Rep. **8**(1), 18029 (2018).
[29] A. Ghaffar, M. A. Alkanhal, Opt. Mater. Express **4**(9), 1756 (2014).

_____
*Corresponding author: aghaffar16@uaf.edu.pk